



Title	The Formation Mechanism of a Thick Cloud Band over the Northern Part of the Sea of Japan during Cold Air Outbreaks
Author(s)	Ohtake, Hideaki; Kawashima, Masayuki; Fujfyoshi, Yasushi
Citation	Journal of the Meteorological Society of Japan, 87(2), 289-306 <a href="https://doi.org/10.2151/jmsj.87.289">https://doi.org/10.2151/jmsj.87.289</a>
Issue Date	2009-04
Doc URL	<a href="http://hdl.handle.net/2115/38898">http://hdl.handle.net/2115/38898</a>
Type	article
File Information	87-2_p289-306.pdf



[Instructions for use](#)

## The Formation Mechanism of a Thick Cloud Band over the Northern Part of the Sea of Japan during Cold Air Outbreaks

Hideaki OHTAKE

*Graduate School of Environmental Earth Science, Hokkaido University, Sapporo, Japan*

Masayuki KAWASHIMA

*Institute of Low Temperature Science, Hokkaido University, Sapporo, Japan*

and

Yasushi FUJIYOSHI

*Institute of Low Temperature Science, Hokkaido University, Sapporo, Japan*  
*Frontier Research System for Global Change, Yokohama, Japan*

*(Manuscript received 25 April 2008, in final form 30 December 2008)*

### Abstract

During cold-air outbreaks in winter, a thick cloud band frequently appears over the northern Sea of Japan and produces localized heavy snowfall in the western coastal region of Hokkaido Island, northern part of Japan. The formation mechanism of this thick cloud band is investigated through a series of nonhydrostatic numerical simulations with a horizontal grid spacing of 5 km. The control simulation well reproduces the characteristics of an observed cloud band. The cloud band forms between relatively warm north-northwesterly winds on the north-east side and relatively cold northwesterly winds on the southwest side. Sensitivity experiments in which upstream topography is modified indicate that the formation and intensification of the cloud band depend on the following two effects; one is the effect of a specific mountain located near the coastline in the middle part of Russia's Sikhote-Alin mountain range (SAMR), and the other is the effect of large-scale topography along the SAMR on synoptic-scale low-level cold northwesterlies.

The specific mountain deflects the cold airflow and immediately a convergence zone forms downstream of the specific mountain, where the cloud band is initiated. On the northeastern side of this mountain, the Froude number is estimated to be about 0.4 from relatively high topography ( $\sim 1.2$  km), stable stratification ( $\sim 0.02$  s $^{-1}$ ), and synoptic-scale wind speed of 10 m s $^{-1}$ . Thus, the relatively high topography strongly blocks a low-level cold air, whereas an upper air with high potential temperature flows downward over the sea. In contrast, on the southwestern side of the mountain, a low-level cold air can pass over the topography, because the Froude number is estimated to be about 1.6 from relatively low topography ( $\sim 0.8$  km) and weak stable stratification ( $\sim 0.008$  s $^{-1}$ ). These two airs with different potential temperature create a mesoscale frontal zone over the sea, which causes the further development of the thick cloud band initiated by the coastal specific mountain in the SAMR.

---

Corresponding author and present affiliation: Hideaki Ohtake, Meteorological Research Institute, 1-1 Nagamine, Tsukuba, Ibaraki 305-0052, Japan.  
E-mail: hiohtake@mri-jma.go.jp  
© 2009, Meteorological Society of Japan

### 1. Introduction

When a continental cold air breaks out from the east coast of the Eurasian Continent over the Sea of Japan in winter, many cloud streets and cloud

bands develop over the sea. Satellite images frequently show a single, remarkably broad cloud band over the western Sea of Japan, extending from the base of the Korean Peninsula to the western Japan. Researchers have intensively investigated the structure and formation mechanism of this broad cloud band, which occasionally produces heavy snowfall (e.g., Nagata et al. 1986; Nagata 1987, 1991, 1992; Arakawa et al. 1988; Murakami et al. 2002; Tsuboki and Asai 2004; Yoshizaki et al. 2004; Ohigashi and Tsuboki 2007).

Early studies suggested that the broad cloud band in the western Sea of Japan was a kind of mesoscale front that formed from the convergence of two air flows with different degrees of transformation, i.e., relatively cold westerly flow passing the Korean Peninsula (on the southwestern side) and relatively warm northerly one from the Vladivostok area (on the northeastern side) (e.g., Okabayashi 1972; Hozumi and Magono 1984). This mechanism is similar to that proposed by Atlas et al. (1983), who showed that the coastline shape could have a profound effect on the establishment of a convergence line over the sea because of differential heating caused by different over-water path lengths. On the other hand, Arakawa et al. (1988) and Murakami et al. (2005) reported some cases in which the convergence formed between relatively

warm air flow on the southwestern side of the cloud band and relatively cold one on the northeastern side. Yagi et al. (1986) investigated the structure of the cloud band and suggested that the convergence line associated with the cloud band resulted from a blocking effect of the mountains north of Korea. Numerical experiments by Nagata et al. (1986) indicated that the land-sea contrast of thermal property between the Korean Peninsula and the Sea of Japan also played an important role in the formation of the cloud band. Additional numerical study by Nagata (1991) showed that the relative contributions of the three lower boundary forcings, i.e., the land-sea thermal contrast, the blocking effect of the mountains north of Korea, and the characteristic sea surface temperature (SST) distribution, were equally important for the formation of the cloud band.

Over the northern Sea of Japan, a remarkably thick cloud band oriented roughly in a northwest-southeast direction also frequently appears during outbreaks of cold air. Satellite images clearly show such a cloud band thicker than neighboring bands (i.e., cloud streets) that extends from the sea off the east coast of the Eurasian Continent to Ishikari Bay in Hokkaido (e.g., Fig. 1). This cloud band often forms at the similar location and sometimes brings local heavy snowfall exceeding  $50 \text{ cm day}^{-1}$  along

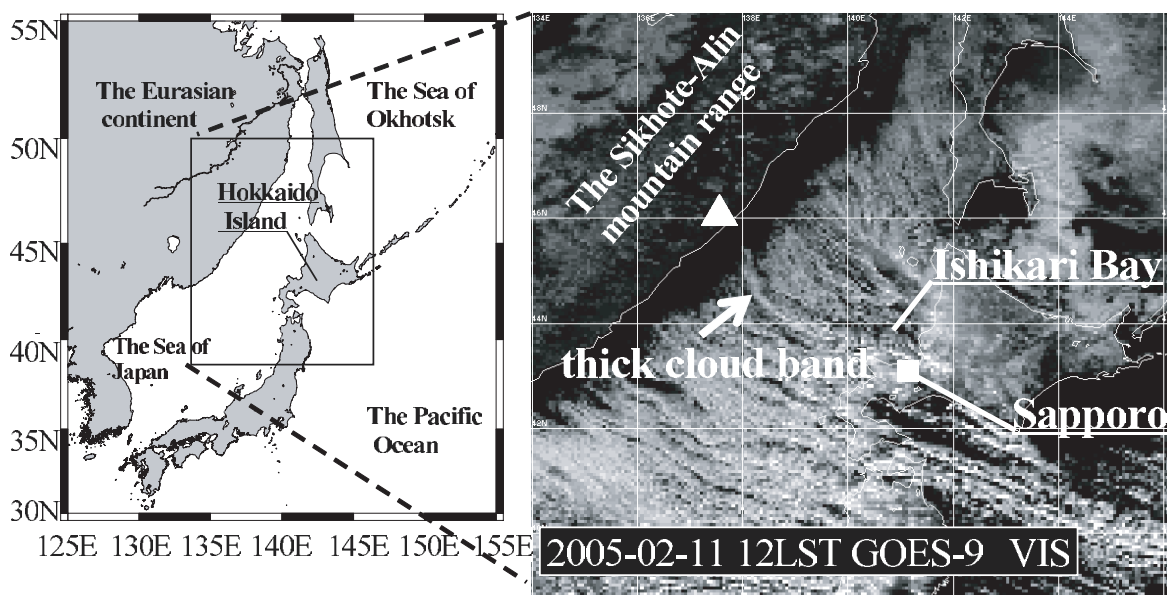


Fig. 1. Map of the area around the Sea of Japan and GOES-9 visible image at 12 LST 11 February 2005. The white arrow indicates the target thick cloud band in the present study. The white triangle denotes the specific mountain (Mt. X) near the coast of Russia's Sikhote-Alin mountain range (SAMR).

the western coast of Hokkaido Island. Muramatsu (1979) pointed out that the initial formation point of this thick cloud band was fixed at the same position, namely the lee side of the specific mountain located at  $137.1^{\circ}\text{E}$ ,  $45.5^{\circ}\text{N}$ . He also suggested that the turbulence created by the upstream mountains was responsible for enhancing the cloud band.

A number of studies were performed using Doppler radar and/or satellite data to investigate the structure of cloud systems in the downwind portion of the thick cloud band (e.g., Fujiyoshi et al. 1992, 1998; Satoh 1994; Katsumata et al. 1998, 2000; Yoshimoto et al. 2000). However, the formation mechanism of the thick cloud band has not been investigated yet, because few data are available for the region where this type of cloud band initiates and develops. Therefore, the main goal of this study is to examine the formation mechanism of the thick cloud band observed off the western coastal region of Hokkaido, by using a numerical model. Especially, this study focuses on the effect of upstream terrain located in Russia's Sikhote-Alin mountain range (SAMR) through a series of sensitivity experiments.

The contents of this paper are organized in the following manner. The characteristics of the target thick cloud band and the surrounding synoptic conditions are presented in Section 2. The numerical model used in this study and their results are described in Sections 3 and 4, respectively. In Section 5, the formation mechanism of the thick cloud band is discussed based on a series of sensitivity experiments. A summary and conclusions are provided in the last section.

## 2. A thick cloud band and environmental conditions

To identify thick cloud band events, visible cloud images were obtained by the Geostationary Meteorological Satellite (GMS) and the Geostationary Operational Environmental Satellite-9 (GOES-9) for 8 winters from 1998 to 2005 (from January to March in 1998 and from October to March for other winters). Among the 1326 days investigated, the thick cloud bands of interest, defined as an almost stationary cloud band whose initial formation point was fixed at the lee side of the specific mountain located at  $137.1^{\circ}\text{E}$ ,  $45.5^{\circ}\text{N}$ , were identified for 261 days. In this study, the thick cloud band that occurred on 11 February 2005 (Fig. 1) is chosen for numerical examinations because the thick cloud band stagnated for longer than one day, and caused

local heavy snowfall over the western coastal region of Hokkaido.

Figure 2 shows the surface synoptic charts for 21 LST 10 February 2005 and 21 LST 11 February 2005, depicted from the National Centers for Environmental Prediction (NCEP) reanalysis data.

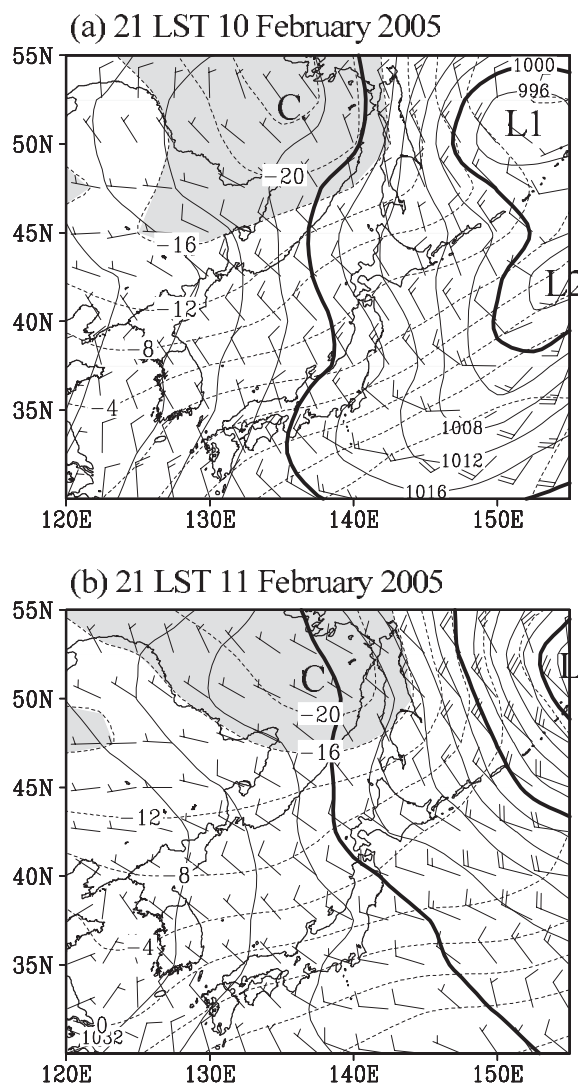


Fig. 2. Time series of surface pressure (thin and thick solid lines at contour intervals of 4 and 20 hPa, respectively); air temperature (broken line; contour interval is 4 K), and wind (barb) at (a) 21 LST 10 February 2005 and (b) 21 LST 11 February 2005. The light shading denoted by the letter "C" indicates  $< -16^{\circ}\text{C}$ . Half-barbs and full-barbs indicate  $5\text{ m s}^{-1}$  and  $10\text{ m s}^{-1}$ , respectively.

Hereafter, the local standard time in Japan (LST = UTC + 9 hours) will be used. The synoptic-scale cyclone is located over the Sea of Okhotsk and the Pacific Ocean, and cold northwesterly winds spread over the Sea of Japan. The cold-air mass with temperature lower than  $-16^{\circ}\text{C}$  is stationary over Siberia from 10 to 11 February 2005. The cold air

outbreak weakens with time beyond 10 February 2005, as suggested by wider intervals of isobars and weaker northwesterly winds over the Sea of Japan at 21 LST 11 February 2005 (see Figs. 2a and 2b).

Figure 3 shows the equivalent blackbody temperature (TBB) at cloud tops at 9-hourly intervals from 12 LST 11 February 2005 to 06 LST 12 February 2005. Although a cloud system located over the northern part of the west coastal region of Hokkaido is most remarkable, a thick cloud band located off the west coast is targeted in this study. The cloud top temperature of the thick cloud band reaches  $-30^{\circ}\text{C}$  in the coldest area. The thick cloud band stagnated for one day and then dissipated at approximately 15 LST 12 February 2005. The thick cloud band undulated until it dissipated (Fig. 3b). However, the initial formation point of the thick cloud band was almost fixed at the specific position ( $137.6^{\circ}\text{E}$ ,  $45.2^{\circ}\text{N}$ ).

Figure 4 shows the daily precipitation amount derived from operational radar of the Japan Meteorological Agency (JMA) on 11 February 2005. Although clouds almost completely cover the western coastal region of Hokkaido (Fig. 3), precipitation (snowfall) is concentrated in only two regions. The

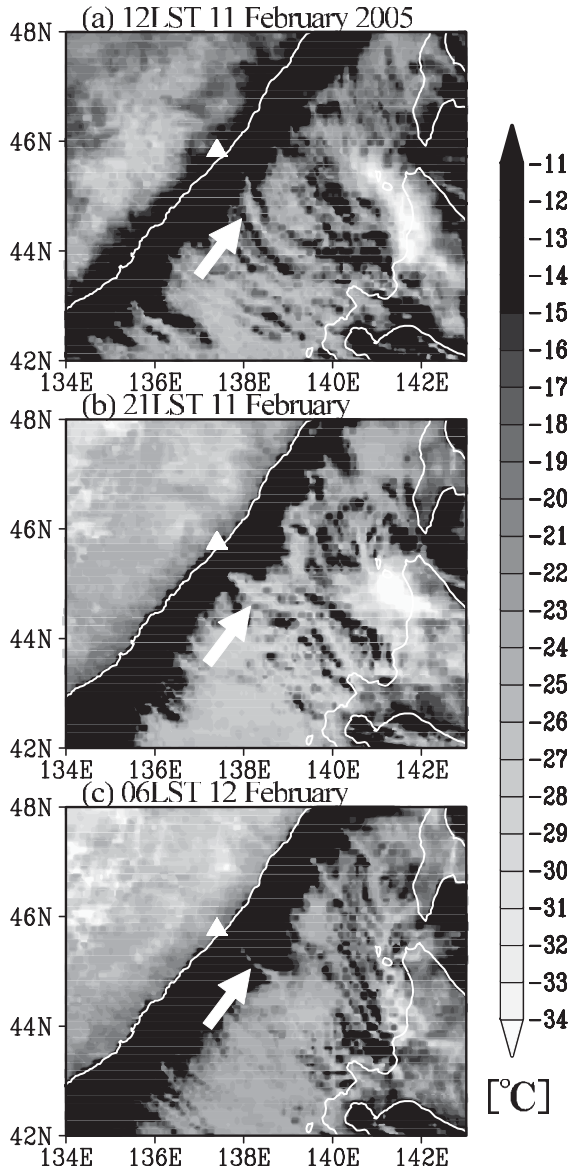


Fig. 3. Time series of GOES-9 infrared images for (a) 12 LST 11 February 2005, (b) 21 LST 11 February 2005 and (c) 06 LST 12 February 2005. The color scale of equivalent black body temperature (TBB;  $^{\circ}\text{C}$ ) is shown on the right side.

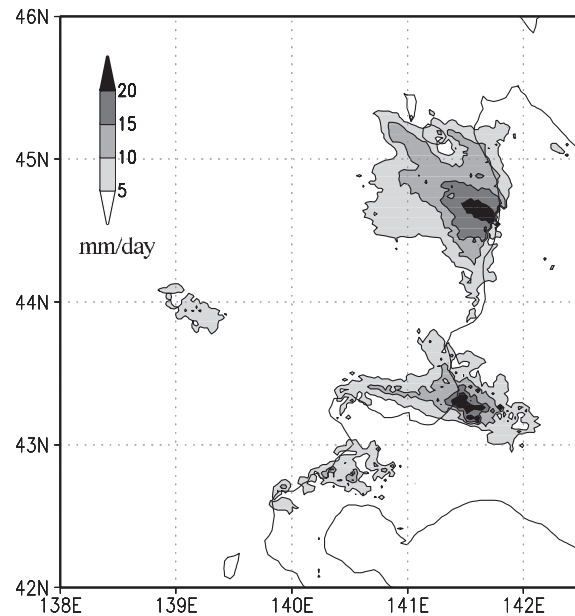


Fig. 4. Daily accumulated precipitation estimated by operational radar data of the Japan Meteorological Agency on 11 February 2005.

wider precipitation area around  $44.5^{\circ}\text{N}$  was caused by the aforementioned low TBB cloud system, whereas the other area around  $43.3^{\circ}\text{N}$  was caused by the target thick cloud band. The precipitation associated with the thick cloud band was enhanced in a downstream direction over Ishikari Bay in Hokkaido, consistent with previous radar observations of the thick cloud band by Fujiyoshi et al. (1992).

### 3. Numerical model

The numerical simulations were performed using the version 4.5.2 of the Advanced Regional Prediction Systems (ARPS), a three-dimensional nonhydrostatic model developed at the Center for Analysis and Prediction of Storms (CAPS) at the University of Oklahoma. Xue et al. (1995) have provided a comprehensive description of the model.

The model domain size is  $1500 \times 1000 \times 14$  km in the  $x$ ,  $y$ , and  $z$  directions, respectively. The horizontal grid spacing is 5 km. There are 30 vertical levels with vertical grid spacing stretched from 200 m near the surface to 900 m near the top of the model domain. Rigid-lid top boundary conditions are applied together with a Rayleigh damping layer in the uppermost 5 km of the model domain. The cloud microphysics are represented using the cold rain parameterization of Lin et al. (1983). The Coriolis force is included in all experiments presented in this paper.

Figure 5 shows the model domain, the elevation of the topography, and the SST used in the simulations. In this domain, the Sea of Japan widens southward and is surrounded by the east coast of the Eurasian Continent and the islands of Sakhalin and Hokkaido. Orographic data were produced from the Global 30 Arc-Second Elevation data set (GTOPO30). A prominent topographic feature is found in the SAMR, which extends with a length of for approximately 800 km along the eastern coast of the Eurasian Continent. A relatively high mountain chain ( $> 1000$  m in elevation) extends toward the northeast from the middle of the SAMR ( $45^{\circ}\text{N}$ ) (Fig. 5b). Another high mountain area ( $> 1000$  m in elevation) is found in the northwestern part of the simulation domain (approximately  $134^{\circ}\text{E}$ ,  $50^{\circ}\text{N}$ ).

The SST was provided from the climatological February-mean of the Global Sea Ice Coverage and SST (GISST) data set (version 2.3b), provided by the British Atmospheric Data Center. Since the annual variation in SST is small over the northern

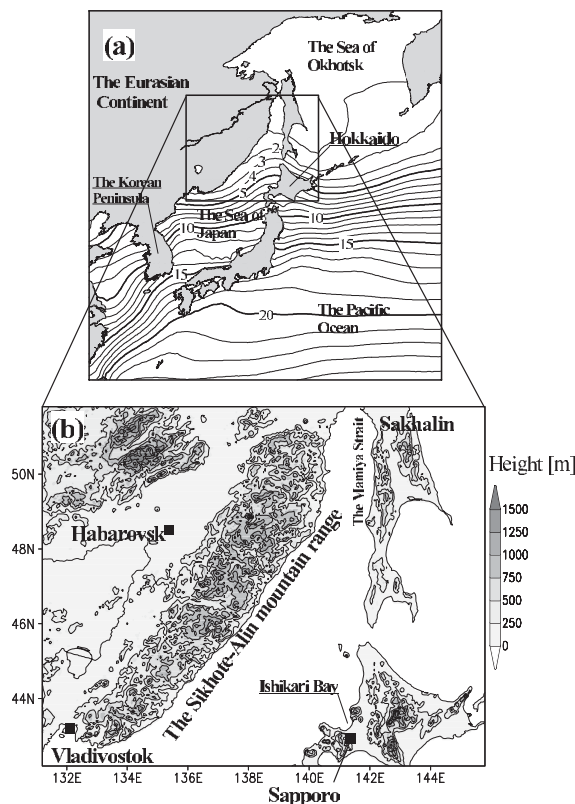


Fig. 5. (a) Map around the Sea of Japan and climatological SST distribution in February. The contour interval is 1 K. (b) Simulation domain and detailed topographic features. The scale of the topography (m) is shown on the right side of the panel; the contour interval is 250 m.

Sea of Japan (not shown), the climatological SST was used as the sea surface boundary condition in this study. The SST was fixed throughout the simulation period. The effect of sea ice was not included as the lower boundary conditions because satellite images during the simulation period showed a rather small extent of sea ice in the model domain. Land-surface temperature was predicted based on an energy budget model.

The initial conditions were prepared by interpolating the NCEP global reanalysis data at 21 LST 10 February 2005 (resolution of  $2.5^{\circ}$  latitude  $\times$  longitude). Additional reanalysis data for every 6 hours were linearly interpolated both temporally and spatially to provide the lateral boundary conditions. The model was integrated for 36 hours. Several sensitivity experiments were also performed

with respect to the effects of upstream topography. The design of the sensitivity experiments is described in Section 5.

#### 4. Results of control simulation

Figure 6 shows the horizontal distributions of the vertically integrated content of the total cloud (sum of cloud water and cloud ice) at 12 LST and 21 LST 11 February 2005 and 06 LST 12 February 2005. A cloud band extends from the sea off the east coast of the Eurasian Continent to the west coastal region of Hokkaido. Although the observed cloud band had some undulations (Fig. 3b), the orientation of the simulated cloud band did not change during the simulation period. The simulated downwind portion of the thick cloud band is shifted slightly southward compared with the satellite images (Fig. 3), and many cloud streaks found in the satellite image are not reproduced because of the coarse model resolution. However, the simulated cloud distributions generally agree well with the observed ones. In particular, the initial formation point of the thick cloud band ( $137.6^{\circ}\text{E}$ ,  $45.1^{\circ}\text{N}$ ) is almost fixed at the same position and well corresponds to that found in the satellite images. Moreover, another remarkable cloud system with low TBB on the northwestern coastal region of Hokkaido is also reproduced successfully. These results show that the numerical simulation well reproduces the observed characteristics of remarkable cloud systems in the target region of this study; therefore, the model results can be used to investigate the formation mechanism of the thick cloud band.

Figure 7 shows the vertical velocity at a 0.5 km above sea level (ASL), potential temperature at a 0.1 km ASL, and horizontal wind vectors at the third vertical grid level (approximately 0.5 km above the ground level) at 12 LST 11 February 2005. Over the Eurasian Continent, northwesterly winds prevail over the simulation domain, except the region with weak winds around  $136^{\circ}\text{E}$ ,  $49^{\circ}\text{N}$ . This weak wind region is caused by tall mountains located in the northwestern part of the simulation domain (around  $134^{\circ}\text{E}$ ,  $50^{\circ}\text{N}$ ; the dotted rectangle shown in Fig. 7), which divide the synoptic-scale winds into two airflows. The remarkable cloud system in the northwestern coastal region of Hokkaido forms in the convergence zone of the divided airflows over the sea (around  $140^{\circ}\text{E}$ ,  $45^{\circ}\text{N}$ ). On the other hand, the target thick cloud band develops in the region where the southern branch of the divided airflows outbreaks over the sea.

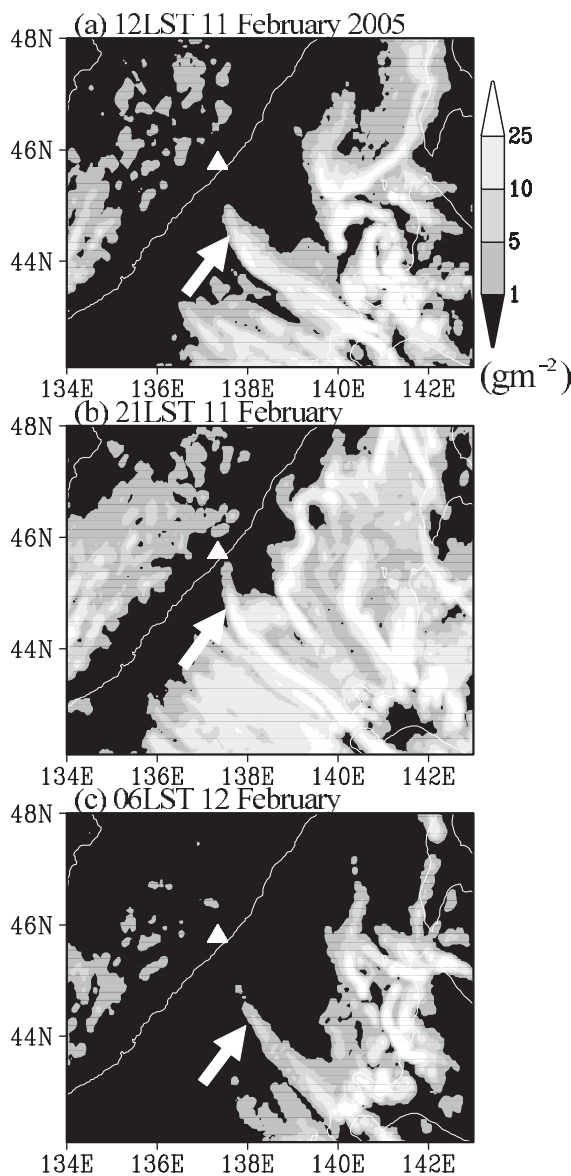


Fig. 6. Time series of the vertically integrated content (shading;  $\text{g m}^{-2}$ ) of the total cloud (sum of cloud water and cloud ice) for the control case for (a) 12 LST 11 February 2005, (b) 21 LST 11 February 2005 and (c) 06 LST 12 February 2005. The bold arrow in each panel indicates the thick cloud band.

Figure 7 also shows that a band-shaped updraft is associated with the thick cloud band (Fig. 6a). The updraft forms on the lee side of a specific mountain near the coastline (around  $45.5^{\circ}\text{N}$ ,  $137.5^{\circ}\text{E}$ ). Hereafter, this mountain is referred to as

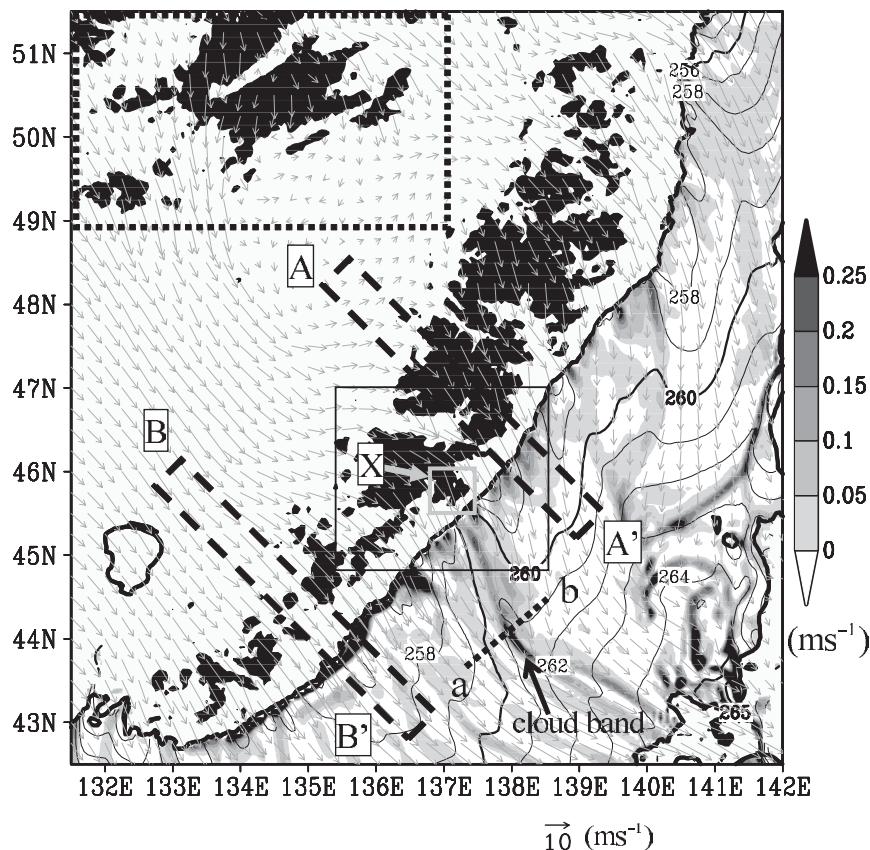


Fig. 7. Upward velocity at a 0.5 km above sea level (ASL; shading;  $\text{m s}^{-1}$ ), potential temperature at a 0.1 km ASL (contour interval is 1 K), and wind vectors at the third vertical grid level (approximately 0.5 km above ground level) for the control case at 12 LST 11 February 2005. The updraft velocity and potential temperature are not shown on the land. The letter “X” denotes the specific mountain near the coast of the SAMR. The contour interval is 1 K, and the potential temperature of 260 K is indicated by a thick line. The dotted line (a-b) indicates the location of the vertical cross-section shown in Fig. 9. The rectangular domains A-A' and B-B' indicate the areas used to construct the vertical cross-sections in Fig. 10. The black shading indicates areas with heights larger than 600 m.

Mt. X. The potential temperature is lower on the southwestern side of the cloud band than on the northeastern side, even though the SST distributes in the opposite sense there (Fig. 5a). On the northeastern and southwestern sides of Mt. X, relatively strong north-northwesterly and northwesterly winds prevail over the SAMR, respectively. These two airflows create a low-level convergence zone over the sea, and the thick cloud band forms along the convergence zone. It should be noted that the topography of the SAMR is generally higher on the upstream side of the relatively warm north-northwesterly winds on the northeastern side of the SAMR than that of the relatively cold northwesterly winds on the southwestern side.

Figure 8 shows the surface pressure over the sea and horizontal wind vectors at the third vertical grid level (approximately 0.5 km above the ground level) for the region enclosed by the black solid rectangle shown in Fig. 7. The wind vectors indicate that the horizontal winds deflect laterally around Mt. X (the dotted rectangle shown in Fig. 8), and the deflected airflows make a convergence zone in the downstream region of Mt. X. The deflected airflows make convergence in response to the reduction of pressure on the immediate lee side of Mt. X. Though not shown, the convergence zone also formed in a sensitivity experiment in which the latent heating associated with the formation of clouds is turned off. This indicates

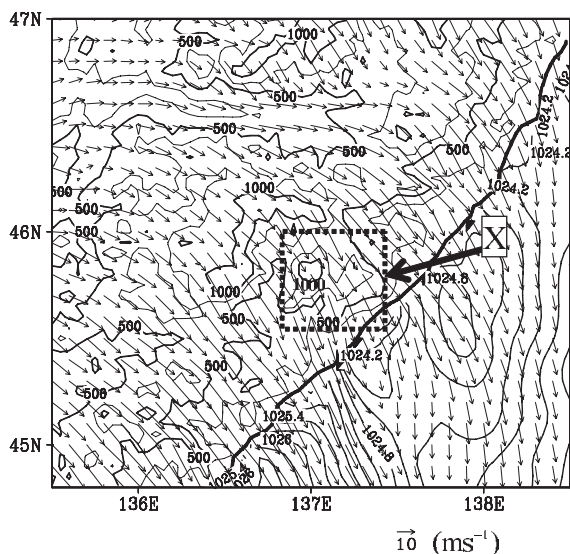


Fig. 8. Close-up view of the region enclosed by the black rectangle in Fig. 7. The contours over the sea are the surface pressure (contour interval is 0.2 hPa) and those on the land are the height of topography (The thin (thick) contour interval is 250 (500) m.). Wind vectors at the third vertical grid level (approximately 0.5 km above ground level) are shown.

that the convergence zone forms mainly by the dynamical effects of the upstream topography.

The above-mentioned features are consistent with those found by numerical studies on the low Froude number flow passing three-dimensional topography (e.g., Smolarkiewicz and Rotunno 1989, 1990). Such topographically-induced disturbance is important for the formation of thick and long cloud streets on the lee sides of islands or coastal mountains (Kang and Kimura 1997). Because Mt. X is not an isolated mountain, the lateral deflection of winds and the lee-side formation of low-level convergence are less clear than those described by Kang and Kimura (1997). However, the qualitative similarity of the simulated wind field between our case and the previous studies suggests that Mt. X triggers the thick cloud band and determines its initial formation point. This suggestion is discussed here.

The vertical structure of the low-level convergence zone along line a-b in Fig. 7 is shown in Fig. 9. The convergence zone has characteristics of a mesoscale front, forming between relatively warm

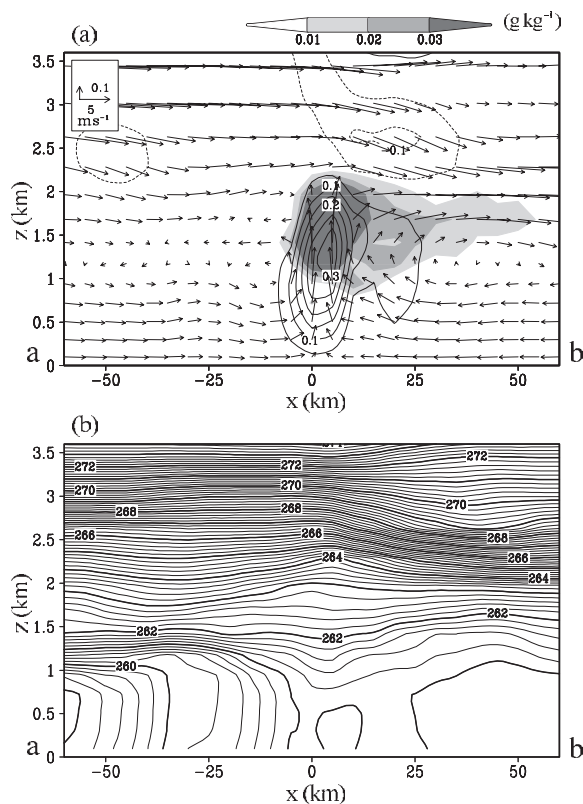


Fig. 9. Vertical cross-sections along dotted line a-b in Fig. 7. (a) Vertical velocity (contour interval is 0.05 m s<sup>-1</sup>) with wind vectors projected in the plane of the cross-section and the total cloud mixing ratio ( $q_c + q_i$ ). Shading denotes the total mixing ratio larger than 0.01 g kg<sup>-1</sup>. (b) The potential temperature. Thick and thin lines represent contour intervals of 1.0 and 0.2 K, respectively.

and cold airs on its northeastern and southwestern sides below a 1 km ASL. The updraft is located at the northeastern edge of the cold air and reaches approximately a 2.2 km ASL.

Figure 10 shows vertical cross-sections of potential temperature and wind vectors along the dashed rectangular domains shown in Fig. 7 (A-A' and B-B'). The variables are averaged over the southwest-northeast span of the rectangular domains. On the northeastern side of the Mt. X (Fig. 10a), the upstream wind speed is very low and the low-level cold air does not climb over the SAMR. On the southwestern side, however, the low-level cold air rises over the SAMR with almost maintaining its traveling speed (Fig. 10b). The potential

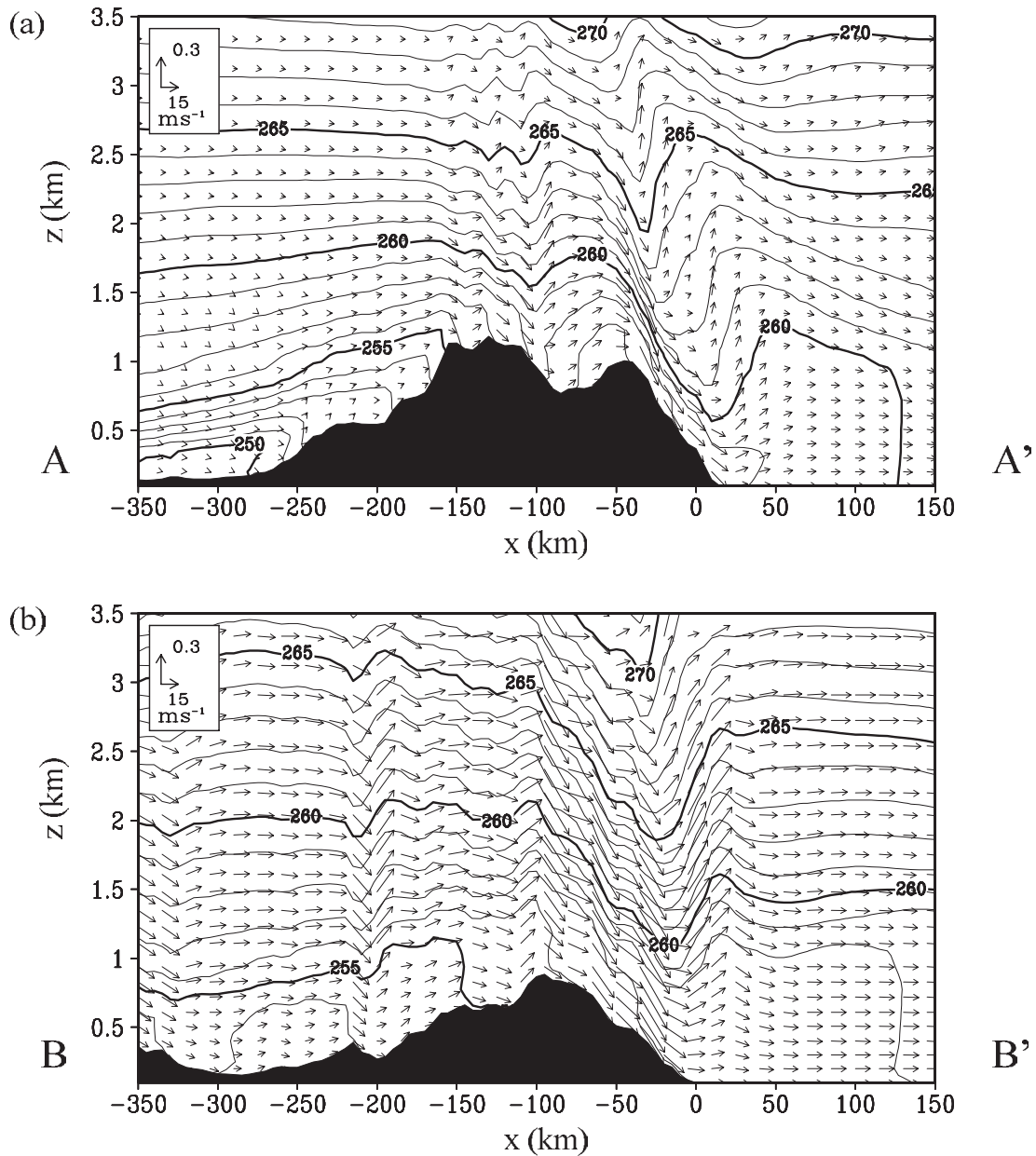


Fig. 10. Vertical cross-sections of potential temperature averaged over the southwest-northeast span of the rectangular domains (a) A-A' and (b) B-B' in Fig. 7 (thick and thin lines indicate contour intervals of 5 K and 1 K, respectively) with wind vectors projected in the plane of the cross-section. The black shading in the figures indicates the topography.

temperature field shows that airs with potential temperature  $> 259$  K can pass over the northeastern part of the SAMR (NEP), whereas airs with potential temperature  $> 257$  K can pass over the southwestern part (SWP). Therefore, the low-level potential temperature on the lee side of the

SAMR is approximately 2 K higher on the northeastern side of the convergence zone over the Sea of Japan than on the southwestern side.

In the case of two-dimensional stratified fluid, the low-level flow is blocked by a mountain when the Froude number  $F_r = U/Nh_m$  is  $< 1$ . Here,  $U$  is

the wind speed,  $N$  is the Brunt Väisälä frequency, and  $h_m$  is the maximum height of the mountain. In the SWP of the present case (Fig. 10b), the wind speed of the low-level northwesterly wind is  $\sim 10 \text{ m s}^{-1}$ , and the Brunt Väisälä frequency of the low-level air over the continent below a height of 1 km is  $\sim 0.008 \text{ s}^{-1}$ . Such an airflow with  $F_r \sim 1.6$  could not be blocked by the mountains with heights of 0.8 km. In contrast, the upstream low-level air is more stably stratified with  $N \sim 0.02 \text{ s}^{-1}$ , and the mountains are taller ( $\sim 1.2 \text{ km}$ ) in the NEP (Fig. 10a). Even if the wind speed is set to that of the synoptic-scale wind ( $\sim 10 \text{ m s}^{-1}$ ), the Froude number in the NEP is estimated to be only  $F_r \sim 0.4$ . Thus, the low-level flow could be blocked by the mountain in the NEP.

Low-level wind vectors cross the isothermal lines in the SWP (Fig. 10b), indicating that diabatic heating occurs there. In the simulation, some clouds formed over the upwind slope of the SWP (not shown), as found in satellite images (Fig. 3). To assess the influence of diabatic heating on the land, a sensitivity experiment is performed excluding the condensational heating on the land and the heat exchange on the land surface. The simulation results (not shown) little change from the control ones (Fig. 10). Therefore, the influence of diabatic heating on the land can be neglected.

## 5. Sensitivity experiments

The results of control simulation (hereafter abbreviated to CNTL) suggest that a specific mountain near the coastline ahead of the SAMR (Mt. X) triggers the thick cloud band and determines its initial formation point. Moreover, the formation of relatively warm north-northwesterly and cold northwesterly winds downstream of the SAMR could also be important for the development of the thick cloud band. To discuss these considerations, several sensitivity experiments are performed by modifying the topography in the SAMR. The initial conditions were also prepared by interpolating the NCEP global reanalysis data at 21 LST 10 February 2005 into the modified grids, and the model used the same boundary conditions as those in CNTL.

### 5.1 Role of a specific mountain over the SAMR

Using satellite images, Muramatsu (1979) investigated the relationship between the location of the thick cloud band and upstream orographic features, and showed that the cloud band formed on the lee

side of Mt. X. This mountain is 1600 m high and has a horizontal scale of approximately 50 km. The simulated thick cloud band is also initiated on the lee side of Mt. X. To examine the influence of Mt. X on the formation of the thick cloud band, a sensitivity experiment with modified orography is performed. Since Mt. X is not a completely isolated mountain, it is difficult to remove it completely from the model topography. Thus, we reduced the height of Mt. X to 50% in the model topography. This simulation is referred to as MT50.

Figure 11a shows the vertical velocity at a 0.5 km ASL and near-surface wind and potential temperature fields for MT50 at 12 LST 11 February 2005. The overall wind and potential temperature fields over the Sea of Japan are roughly the same as those in CNTL. A region of strong temperature gradient also forms between relatively cold northwesterly and warm north-northwesterly winds, along which a band-shaped updraft forms. However, the initial formation points of both the band-shaped updraft and the cloud band (Fig. 11b) are shifted further off the coast and southward in comparison with CNTL (the broken line shown in Fig. 11a). The results of MT50 indicate that the topography of Mt. X is essential in determining the initial formation point of the thick cloud band. However, a convergence zone similar to that found in CNTL forms over the Sea of Japan even when the topography of Mt. X is removed.

### 5.2 Role of large-scale topography

#### a. Formation of frontal zone

The results of CNTL suggest that the temperature difference between the southwestern and northeastern sides of the cloud band is caused by the variable topographic heights of the SAMR, whose topography is generally higher in the NEP ( $\sim 1.2 \text{ km}$ ) than in the SWP ( $\sim 0.8 \text{ km}$ ). To examine this suggestion, another sensitivity experiment is performed. In the sensitivity experiment, the height of the mountain range in the SWP (the region within the gray lines shown in Fig. 12) is set to 150% of that in CNTL, to make the topographic height in the SWP comparable with that in the NEP. This simulation is referred to as SW150.

Figure 12 shows the vertical velocity at a 0.5 km ASL and near-surface wind and potential temperature fields for SW150 at 12 LST 11 February 2005. In the NEP, the wind and potential temperature fields over the sea are similar to those in CNTL. On the other hand, the temperature on the lee side

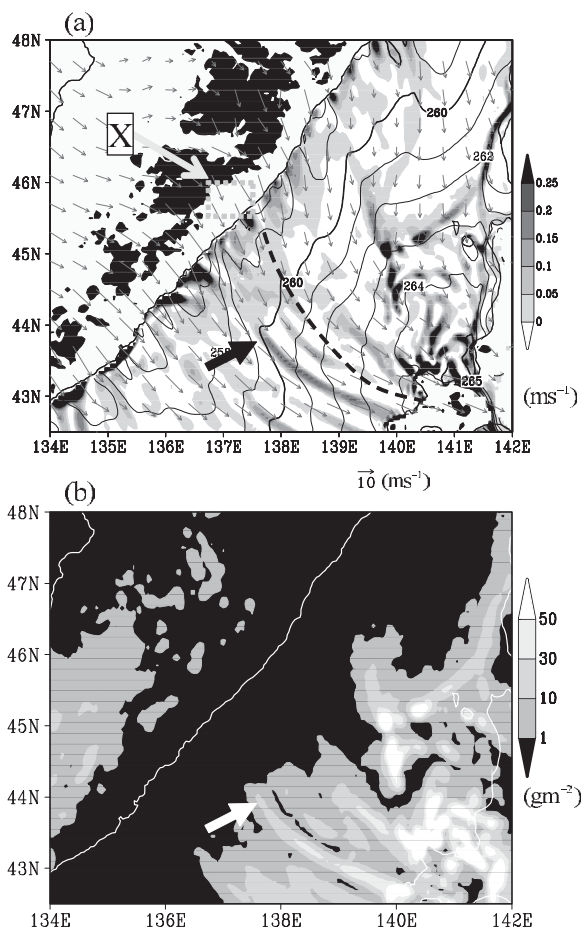


Fig. 11. (a) Upward velocity at a 0.5 km above sea level (ASL; shading;  $\text{m s}^{-1}$ ), potential temperature at a 0.1 km ASL (contour interval is 1 K), and wind vectors at the third vertical grid level (approximately 0.5 km above ground level); (b) Same as Fig 6a, but for MT50. The black bold arrow in (a) and white bold arrow in (b) indicate the thick cloud band, respectively.

of the modified topography (SWP) is higher than that in CNTL, and the low-level winds are deflected more southward. A band-shaped updraft formed in almost the same location as in CNTL. However, the strength of the band-shaped updraft is weaker than that found in CNTL, and other cloud bands, not found in CNTL (Fig. 7), also formed on the lee side of the modified topography.

Figure 13 shows the vertical cross sections of potential temperature and wind vectors for SW150 along the same domains as in Fig. 10. As in Fig.

10a, the upwind-side low-level wind speed normal to the SAMR is low, and low-level cold air does not climb over the NEP (Fig. 13a). Similarly, the low-level cold air does not climb over the SWP (Fig. 13b) and upper-level airs with high potential temperature flow out over the Sea of Japan. The low-level potential temperature on the lee side of the SWP was approximately 2 K lower than that of the NEP in CNTL (Fig. 10), while it is approximately 1 K higher in SW150 (Fig. 13).

The results of SW150 indicate that the formation of a frontal zone between the relatively warm north-northwesterly and relatively cold northwesterly winds on the lee side of the SAMR is important for the development of the thick cloud band. Moreover, the results of SW150 indicate that the variable topographic height of the SAMR, whose height is generally higher in the NEP than in the SWP, is responsible for the formation of the frontal zone over the Sea of Japan.

#### b. Deflection of low-level northwesterly winds

In order to further clarify the effects of the large-scale topography of the SAMR, a sensitivity experiment with smoothed topography (Fig. 14) is also performed. The model topography is smoothed by making a  $100 \times 100$  km spatial running mean to completely remove the topographic effects of small-scale mountains including Mt. X. This simulation is referred to as SMTH.

Figure 15a shows the vertical velocity at a 0.5 km ASL and near-surface wind and potential temperature fields for SMTH at 12 LST 11 February 2005. The overall wind and potential temperature fields over the Sea of Japan are similar to those in CNTL and MT50, although the temperature distribution becomes rather smooth. A band-shaped updraft is found in almost the same location as that in MT50, where the east-west gradient of potential temperature and the vertically-investigated mixing ratio of cloud water and ice are large (Fig. 15b). These results demonstrate that the characteristic winds and thermodynamic fields over the sea are created not by the small-scale topography, but by the large-scale topography of the SAMR.

As in CNTL, northwesterly winds turned southward over the NEP. Therefore, this process is examined from the results of SMTH, in which perturbations caused by many small-scale mountains are absent. Figure 16 shows the vertical cross-sections of potential temperature and relative vertical vorticity along the same domain as that in Fig. 10 for

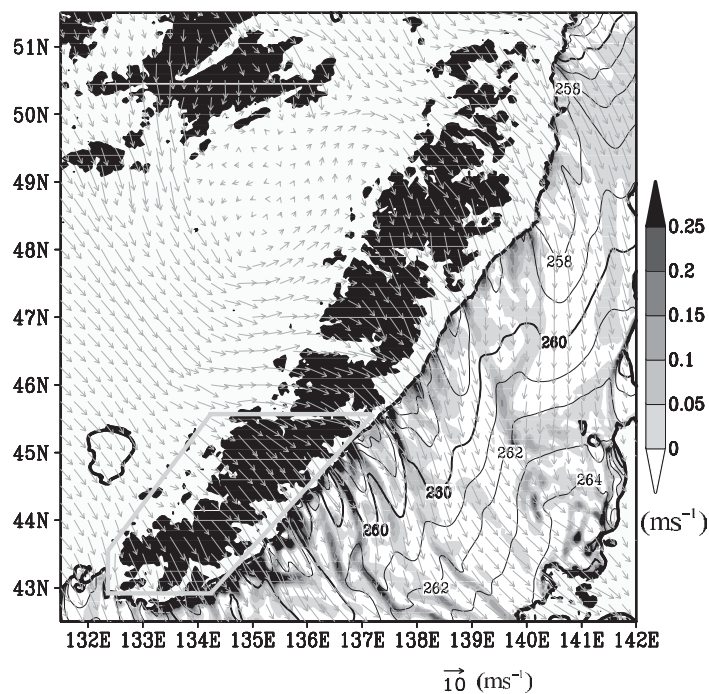


Fig. 12. As in Fig. 7, but for SW150.

SMTH. In the NEP (Fig. 16a), the low-level air is also blocked by the SAMR, and the airflow above a 1 km ASL passes over the SAMR. An area of negative vertical vorticity forms below a 2 km ASL over the SAMR, where the vertical contour interval of potential temperature decreases in a downstream direction.

In the present case, the characteristic Rossby number of the airflow over the SAMR is estimated about 0.3 from the horizontal scale of the SAMR in the wind direction ( $\sim 300$  km), the wind speed of  $10 \text{ m s}^{-1}$ , and the Coriolis parameter of  $1 \times 10^{-4} \text{ s}^{-1}$ . Thus, the airflow over the SAMR is affected substantially by the Coriolis effect, and here this effect on the clockwise deflection of the northwesterly winds over the NEP is examined qualitatively by the conservation of potential vorticity in an orographically disturbed stratified flow.

Figure 16a shows that the depth of the air column between the potential temperature surfaces of 258 K and 262 K at  $X = -300$  km, defined as  $h_1$ , is about 0.7 km, where the mean relative vertical vorticity in the column  $\zeta_1$  is about  $-0.6 \times 10^{-5} \text{ s}^{-1}$ . In contrast, the depth of the air column at  $X = -200$  km, defined as  $h_2$ , is about 0.6 km, and the mean relative vertical vorticity in

the column  $\zeta_2$  is about  $-1 \times 10^{-5} \text{ s}^{-1}$ . In the present case, the spatial variation of the Coriolis parameter  $f$  over the area shown in Fig. 16 is small. Therefore, the expected change in relative vorticity  $\Delta\zeta$  associated with the vertical shrinkage of the air column moving from  $X = -300$  km to  $X = -200$  km is estimated to be about  $-1.3 \times 10^{-5} \text{ s}^{-1}$  from  $\Delta\zeta = (f + \zeta_1) \times (h_2 - h_1)/h_1$ . Although the difference of  $\zeta_1$  and  $\zeta_2$  ( $-0.4 \times 10^{-5} \text{ s}^{-1}$ ) calculated from simulation results is considerably smaller than the estimated value because of the surface friction and diffusion, the clockwise deflection of northwesterly winds over the NEP could be associated with the vertical shrinkage of air column over the SAMR. Moreover, this vertical shrinkage accompanies the acceleration of northwesterly wind speed over the NEP, as found in Fig. 16a. Therefore, the clockwise deflection of northwesterly winds can also be explained by the enhancement of the southwestward Coriolis force associated with the acceleration of northwesterly wind speed.

The anticyclonic relative vorticity over the SAMR is considerably smaller in the SWP than that in the NEP (Fig. 16b). This is because the up-wind slope of the SAMR is smoother in the SWP

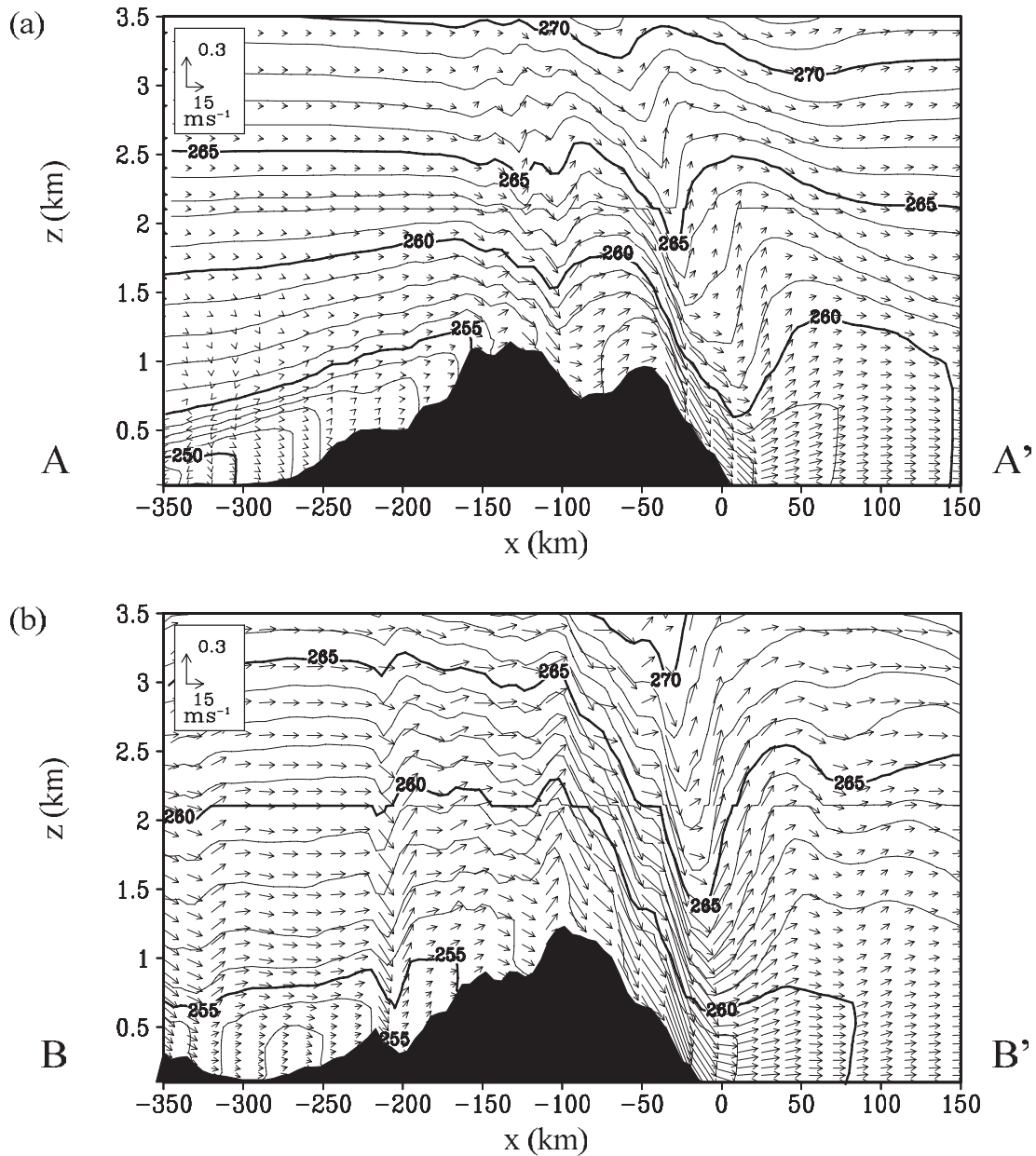


Fig. 13. As in Fig. 10, but for SW150.

than in the NEP, and therefore the vertical shrinkage of the low-level air column is less significant in the SWP than in the NEP.

The large-scale topography of the SAMR is relatively low in the region north of  $49.5^\circ\text{N}$  (lower than 600 m), compared with that in the central part ( $47\sim 49.5^\circ\text{N}$ , see Fig. 14). In that region, low-level cold northwesterly winds pass over the SAMR and flow out over the sea. However, the low-level cold

northwesterly winds significantly deflect southward, while such a deflection is not found over the SWP. In the present case, since the characteristic Rossby number of the airflow ( $\sim 0.3$ ) is not sufficiently small, the ageostrophic motion is not negligible. Here, the ageostrophic effect on the deflection of northwesterly winds is estimated from the motion of airflow passing three-dimensional topography in a non-rotating atmosphere.

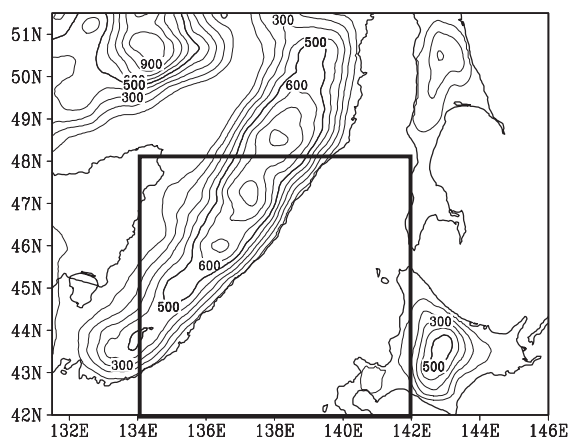


Fig. 14. Topographic features in SMTH. The thick and thin contour lines have intervals of 500 and 100 m, respectively. The rectangular domain indicates the area in Fig. 15.

In the non-rotating atmosphere, the low-level northwesterly winds in the region north of  $49.5^{\circ}\text{N}$  would turn anticyclonically around the high-altitude region located to the southwest, as in the simulation of low Froude number flow passing three-dimensional topography. This anticyclonic rotation tendency, combined with the enhancement of anticyclonic vorticity associated with the vertical shrinkage of the air column in a rotating atmosphere, could cause the significant southward deflection of northwesterly winds. On the other hand, the low-level northwesterly winds over the SWP would turn cyclonically around the high-altitude region located to the northeast in a non-rotating atmosphere. This cyclonic rotation tendency would suppress the enhancement of anticyclonic vorticity associated with the vertical shrinkage of the air column, which could be the reason for a little deflecting the low-level northwesterly winds over the SWP.

In all simulations described above, the low-level upstream airs were more stably stratified in the NEP than in the SWP. Moreover, it appears that not only variation in topographic height along the SAMR, but also high mountains in the northwestern part of the simulation domain (the region enclosed by the dotted rectangle shown in Fig. 7) might contribute to the variation of low-level wind speed upwind of the SAMR. To examine the influence of the topography of high mountains in the northwestern part of the simulation domain, an

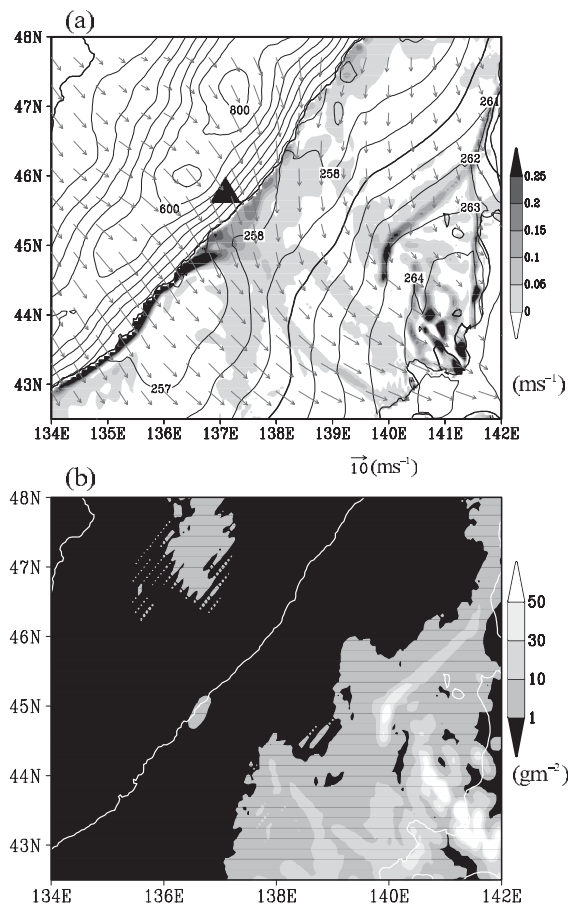


Fig. 15. As in Fig. 11, but for SMTH at 12 LST 11 February 2005. The thin contours in (a) indicate the topography (contour interval is 100 m). The triangle denotes the location of the specific mountain (Mt. X) existing in CNTL.

idealized sensitivity experiment was additionally performed by removing it (not shown). In that experiment, uniform northwesterly winds of  $10\text{ m s}^{-1}$  were set throughout the simulation domain and the Brunt Väisälä frequency of the atmosphere was set to be  $0.01\text{ s}^{-1}$  throughout the troposphere. This experiment somewhat enhanced northwesterly winds on the upstream side of the NEP in comparison with that in CNTL. However, the blocking of low-level cold airs still occurred on the upstream side of the NEP, and simulated temperature and wind fields on the lee side of the SAMR were qualitatively the same as those found in CNTL. Therefore, the influence of the high topography in the northwestern part of the simulation domain is very small.

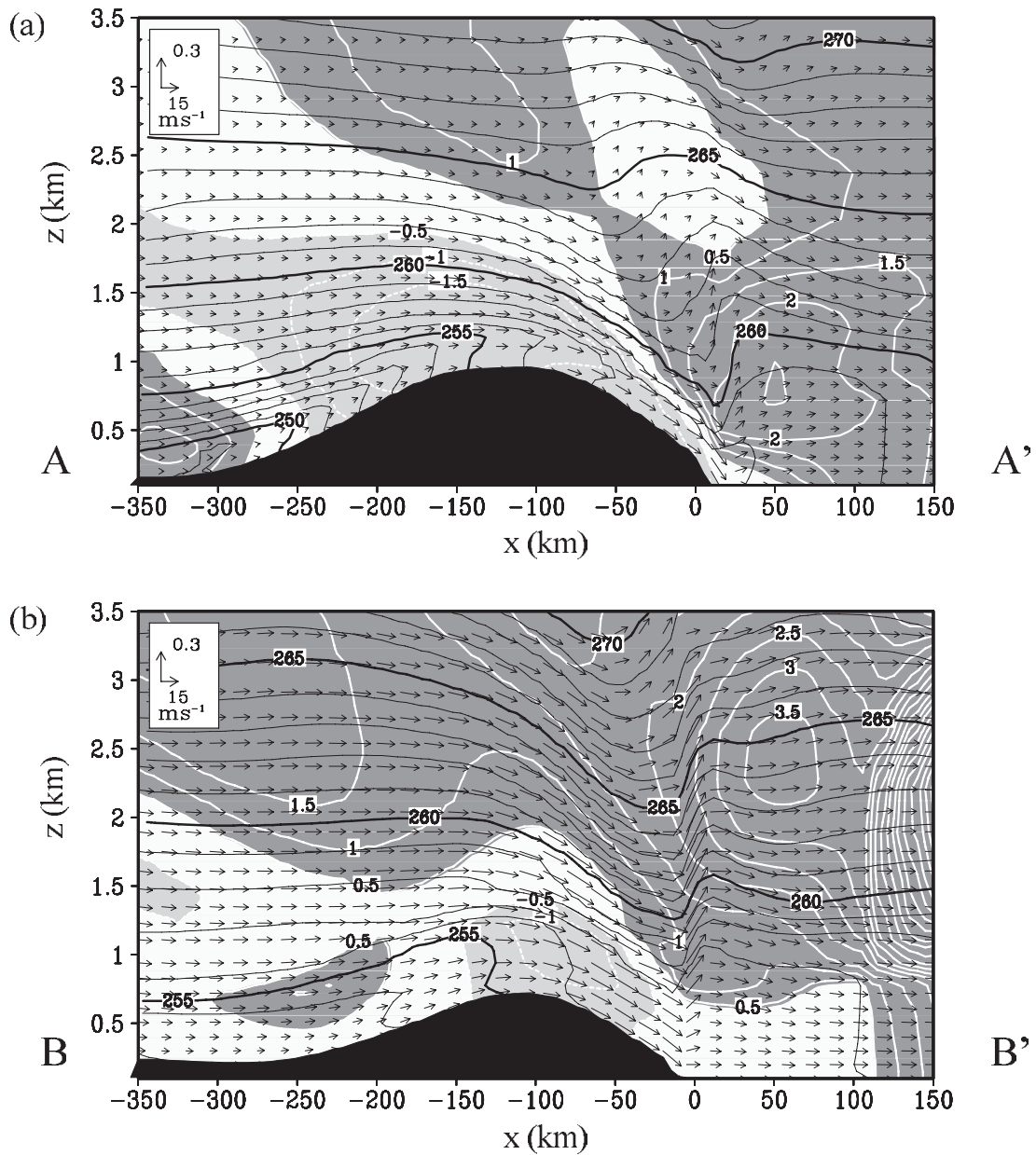


Fig. 16. Northwest-southeast vertical cross-sections across the (a) northeastern and (b) southwestern parts of the SAMR in SMTH, showing potential temperature (thick and thin solid contour lines have intervals of 5 and 1 K, respectively) and vertical relative vorticity (thin white contour line with interval of  $0.5 \times 10^{-5} \text{ s}^{-1}$ ), with wind vectors projected in the plane of the cross-section. The locations of the cross-sections shown in (a) and (b) are the same as those in Figs. 10a and 10b, respectively. Light (dark) shading denotes areas where the vertical component of relative vorticity is smaller (larger) than  $-0.5 \times 10^{-5} \text{ s}^{-1}$  ( $0.5 \times 10^{-5} \text{ s}^{-1}$ ). The black shading indicates the topography.

### 6. Summary and conclusions

A thick cloud band is frequently observed over the northern part of the Sea of Japan during cold-

air outbreaks from the Eurasian Continent, as first noted by Muramatsu (1979). The formation mechanism of the thick cloud band was investigated through a series of numerical simulations using a

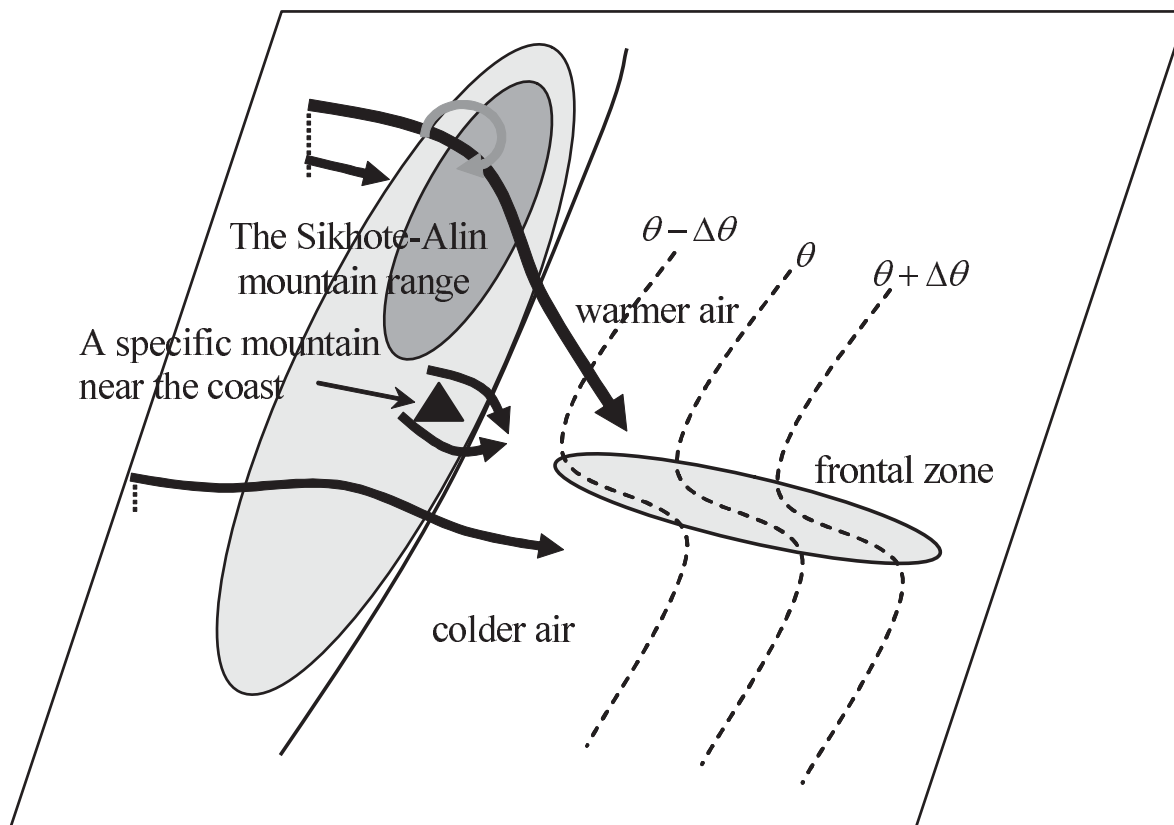


Fig. 17. Schematic illustration of the formation mechanism of the thick cloud band. The triangle denotes the specific mountain (Mt. X) near the coast of the SAMR. The thick solid arrows denote large-scale winds disturbed by the SAMR, while the thin solid arrows denote low-level winds disturbed by Mt. X. The dashed lines denote contours of low-level potential temperature over the Sea of Japan.

nonhydrostatic model with a horizontal grid-spacing of 5 km. The target thick cloud band in the present study was observed on 11 February 2005 and lasted for longer than one day, causing locally heavy snowfall over the western coastal region of Hokkaido, northern part of Japan.

The control simulation well reproduced the characteristics of the thick cloud band. The cloud band formed on the lee side of a specific mountain (Mt. X) noted by Muramatsu (1979) that was located near the coast in the middle part of the Russia's Sikhote-Alin mountain range (SAMR). Relatively warm north-northwesterly and cold northwesterly winds, respectively, prevailed on the northeastern and southwestern sides of the thick cloud band, and a frontal structure was identified across the thick cloud band.

Sensitivity experiments, in which the topography

of the SAMR was modified, showed that Mt. X triggered the thick cloud band and determined its initial formation point. Different blocking of the synoptic-scale low-level cold northwesterly winds between the northeast and southwest parts of the SAMR resulted in the formation of the frontal zone over the Sea of Japan.

Figure 17 schematically illustrates the formation mechanism of the thick cloud band. Mt. X deflects the cold airflow laterally, and a convergence zone immediately forms over the sea on the lee side of Mt. X, where a band-shaped updraft is initiated. On the northeastern side of Mt. X, the Froude number is estimated to be about 0.4 from relatively high topography ( $\sim 1.2$  km), stable stratification ( $\sim 0.02$  s $^{-1}$ ), and synoptic-scale wind speed of 10 m s $^{-1}$ . Thus, the SAMR strongly blocks low-level cold airs, while an upper-level airflow with

high potential temperature breaks out over the Sea of Japan. This airflow is deflected clockwise over the SAMR due to the vertical shrinkage of the air column. In contrast, relatively low mountains on the southwestern side of Mt. X do not block low-level cold airmass. Relatively warm north-northwesterly winds on the northeastern side and cold northwesterly ones on the southwestern side create a frontal zone over the Sea of Japan, where the thick cloud band initiated by Mt. X develops further.

Previous studies have noted that the formation of a frontal zone due to different heating associated with variation in over-water path length is important in generating thick cloud bands over oceans or large lakes (e.g., Kelly 1982; Atlas et al. 1983; Hjelmfelt and Braham 1983; Nagata 1986). However, the formation mechanism of the frontal zone in the present study differs from that in the previous studies; the temperature contrast associated with the thick cloud band is caused by the different blocking effects between the northeastern and southwestern parts of the SAMR on synoptic-scale low-level cold northwesterly winds, not by the variation in over-water path length.

The previous observational studies indicated that the thick cloud band was composed of active convective cells (e.g., Fujiyoshi et al. 1998; Yoshimoto et al. 2000). To better understand the structure and dynamics of the cloud band and its interaction with neighboring cloud streets, simulations with much finer resolution are needed. Future studies must also be made to systematically examine the dependence of the structure and evolution of the thick cloud band on environmental conditions such as the strength and direction of synoptic-scale winds. These are in our future issues.

#### Acknowledgments

We are grateful to Drs. A. Kubokawa and H. Mitsudera of Hokkaido University, Dr. K. Tsuboki of Nagoya University, for their valuable comments. We would also like to thank Dr. T. Kato of the Meteorological Research Institute and two anonymous reviewers for their helpful comments on the manuscript. The numerical experiments were conducted using the Advanced Regional Prediction System (ARPS) version 4.5.2 developed by the Center for Analysis and Prediction of Storms (CAPS), University of Oklahoma. Generic Mapping Tools (GMT) and Grid Analysis and Display System (GrADS) software were used to draw the figures.

#### References

- Arakawa, S., and Research Group on Mesoscale Meteorology of Marine Development, JMA, 1988: On the mesoscale structure of the cloud band system over the Japan Sea in winter monsoon period.—A mesoscale observation on board R/V Keifu-Marui. *Tenki*, **35**, 237–248 (in Japanese).
- Atlas, D., S. Chou, and W. Byerly, 1983: The influence of coastal shape on winter mesoscale air-sea interaction. *Mon. Wea. Rev.*, **111**, 245–252.
- Fujiyoshi, Y., K. Tsuboki, S. Satoh, and G. Wakahama, 1992: Three dimensional radar echo structure of a snow band formed on the lee side of a mountain. *J. Meteor. Soc. Japan*, **70**, 11–24.
- Fujiyoshi, Y., N. Yoshimoto, and T. Takeda, 1998: A dual-Doppler radar study of longitudinal-mode snowbands. Part I: A three-dimensional kinematic structure of meso- $\gamma$ -scale convective cloud systems within a longitudinal-mode snowband. *Mon. Wea. Rev.*, **126**, 72–91.
- Hjelmfelt, M. R., and R. R. Braham, Jr., 1983: Numerical simulations of the airflow over Lake Michigan for a major lake-effect snow event. *Mon. Wea. Rev.*, **111**, 205–219.
- Hozumi, K., and C. Magono, 1984: The cloud structure of convergent cloud bands over the Japan Sea in winter monsoon period. *J. Meteor. Soc. Japan*, **62**, 522–533.
- Kang, S.-D., and F. Kimura, 1997: A numerical study on the mechanism of cloud-street formation in the lee of an isolated mountain near a coast. *J. Meteor. Soc. Japan*, **75**, 955–968.
- Katsumata, M., H. Uyeda, and K. Kikuchi, 1998: Characteristics of a cloud band off the west coast of Hokkaido Island as determined from AVHRR/NOAA, SSM/I and radar data. *J. Meteor. Soc. Japan*, **76**, 169–189.
- Katsumata, M., H. Uyeda, K. Iwanami, and G. Liu, 2000: The response of 36- and 89- GHz microwave channels to convective snow clouds over ocean: Observation and modeling. *J. Appl. Meteor.*, **39**, 2322–2335.
- Kelly R. D., 1982: A single Doppler radar study of horizontal-roll convection in a lake-effect snow storm. *J. Atmos. Sci.*, **39**, 1521–1531.
- Lin, Y.-L., R. D. Farley, and H. D. Orville, 1983: Bulk parameterization of the snow field in a cloud model. *J. Climate. Appl. Meteor.*, **22**, 1065–1092.
- Murakami, M., M. Hoshimoto, N. Orikasa, H. Horie, H. Okamoto, H. Kuroiwa, H. Minda and K. Nakamura, 2002: Inner structures of snow bands associated with the Japan Sea Polar-airmass Convergence Zone based on aircraft observations. *Int. Conf. Mesoscale Convective Systems and Heavy Rainfall/Snowfall in East Asia*, held at Tokyo, 2002, 522–527.

- Murakami, M., M. Hoshimoto, N. Orikasa, Y. Takayama, H. Kuroiwa, H. Horie, H. Okamoto, H. Kamei, and H. Minda, 2005: Inner structures of snow band associated with the Japan-Sea Polar-Airmass Convergence Zone based on aircraft observations. *Meteor. Res. Notes*, **208**, 251–264 (in Japanese).
- Muramatsu, T., 1979: The cloud line enhanced by upwind orographic features in winter monsoon situations. *Geophys. Mag.*, **38**, 1–15.
- Nagata, M., M. Ikawa, S. Yoshizumi, and T. Yoshida, 1986: On the formation of a convergent cloud band over the Japan Sea in winter; Numerical experiments. *J. Meteor. Soc. Japan*, **64**, 841–855.
- Nagata, M., 1987: On the structure of a convergent cloud band over the Japan Sea in winter; a prediction experiment. *J. Meteor. Soc. Japan*, **65**, 871–883.
- Nagata, M., 1991: Further numerical study on the formation of the convergent cloud band over the Japan Sea in winter. *J. Meteor. Soc. Japan*, **69**, 419–427.
- Nagata, M., 1992: Modeling case study of the Japan-Sea convergent cloud band in a varying large-scale environment: Evolution and upscale effect. *J. Meteor. Soc. Japan*, **70**, 649–671.
- Ohigashi, T., and K. Tsuboki, 2007: Shift and intensification processes of the Japan-Sea Polar-Airmass Convergence Zone associated with the passage of a mid-tropospheric cold core. *J. Meteor. Soc. Japan*, **85**, 633–662.
- Okabayashi, T., 1972: Snow cloud seen from meteorological satellites and their application to research on snowfall. *Kishyo Kenkyu Note*, **113**, 74–106 (in Japanese).
- Satoh, S., 1994: Structure of convective cloud bands transverse to the winter monsoon over the Japan sea. Ph.D. thesis, University of Hokkaido (in Japanese), 126 pp.
- Smolarkiewicz, P. K., and R. Rotunno, 1989: Low Froude number flow past three-dimensional obstacles. Part I: Baroclinically generated lee vortices. *J. Atmos. Sci.*, **46**, 1154–1164.
- Smolarkiewicz, P. K., and R. Rotunno, 1990: Low Froude number flow past three-dimensional obstacles. Part II: Upwind flow reversal zone. *J. Atmos. Sci.*, **47**, 1498–1511.
- Tsuboki, K., and T. Asai, 2004: The multi-scale structure and development mechanism of mesoscale cyclones over the Sea of Japan in winter. *J. Meteor. Soc. Japan*, **82**, 597–621.
- Xue, M., K. K. Droegemeier, V. Wong, A. Shapiro, and K. Brewster, 1995: ARPS version 4.0 User's Guide. Available from Center for Analysis and Prediction of Storms, University of Oklahoma, Norman OK 73072. 380 pp.
- Yagi, S., T. Muramatsu, T. Uchiyama, and N. Kurokawa, 1986: “Convergent cloud band” and “Cu-Cb line” over Japan Sea affected by topographic features in the coast of the Asian continent. *Tenki*, **33**, 453–465 (in Japanese).
- Yoshimoto, N., Y. Fujiyoshi, and T. Takeda, 2000: A dual-Doppler radar study of longitudinal-mode snowbands. Part II: Influence of the kinematics of a longitudinal-mode snowband on the development of an adjacent snowband. *J. Meteor. Soc. Japan*, **78**, 381–403.
- Yoshizaki, M., T. Kato, H. Eito, S. Hayashi, and W. Tao, 2004: An overview of the field experiment “Winter mesoscale convective systems (MCSs) over the Japan sea in 2001”, and comparisons of the cold-air outbreak case (14 January) between analysis and a non-hydrostatic cloud-resolving model. *J. Meteor. Soc. Japan*, **82**, 1365–1387.